

Phase Behavior of Ag_2CrO_4 under Compression: Structural, Vibrational, and Optical Properties

David Santamaría-Pérez,^{*,†,‡} Enrico Bandiello,[†] Daniel Errandonea,[†] Javier Ruiz-Fuertes,^{†,§} Oscar Gomis,^{||} Juan Angel Sans,[⊥] Francisco Javier Manjón,[⊥] Plácida Rodríguez-Hernández,[#] and Alfonso Muñoz[#]

[†]Departamento de Física Aplicada-ICMUV, MALTA Consolider Team, Universidad de Valencia, C/Dr. Moliner 50, Burjassot, 46100 Valencia, Spain

[‡]Departamento de Química Física I, Universidad Complutense de Madrid, MALTA Consolider Team, Avenida Complutense s/n, 28040 Madrid, Spain

[§]Lyman Laboratory of Physics, Harvard University, Cambridge, Massachusetts 02138, United States of America

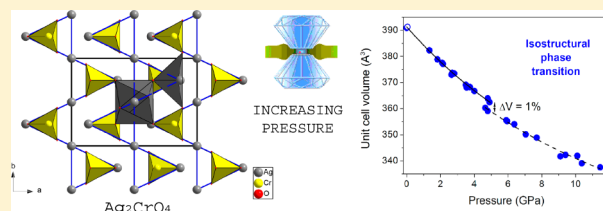
^{||}Centro de Tecnologías Físicas: Acústica, Materiales y Astrofísica, MALTA Consolider Team, Universitat Politècnica de València, 46022 València, Spain

[⊥]Instituto de Diseño para la Fabricación y Producción Automatizada, MALTA Consolider Team, Universitat Politècnica de València, 46022 València, Spain

[#]Departamento de Física Fundamental II, Instituto de Materiales y Nanotecnología, MALTA Consolider Team, Universidad de La Laguna, 38205 Tenerife, Spain

ABSTRACT: We have performed an experimental study of the crystal structure, lattice dynamics, and optical properties of silver chromate (Ag_2CrO_4) at ambient temperature and high pressures. In particular, the crystal structure, Raman-active phonons, and electronic band gap have been accurately determined. When the initial orthorhombic $Pnma$ Ag_2CrO_4 structure (phase I) is compressed up to 4.5 GPa, a previously undetected phase (phase II) has been observed with a 0.95% volume collapse.

The structure of phase II can be indexed to a similar orthorhombic cell as phase I, and the transition can be considered to be an isostructural transition. This collapse is mainly due to the drastic contraction of the a axis (1.3%). A second phase transition to phase III occurs at 13 GPa to a structure not yet determined. First-principles calculations have been unable to reproduce the isostructural phase transition, but they propose the stabilization of a spinel-type structure at 11 GPa. This phase is not detected in experiments probably because of the presence of kinetic barriers. Experiments and calculations therefore seem to indicate that a new structural and electronic description is required to model the properties of silver chromate.



1. INTRODUCTION

Silver chromate has been extensively studied under ambient conditions because of its unusual red color, which makes this compound unique as a pigment and for coloring applications.^{1,2} Although it remains a controversial subject, some authors concluded that the intense absorption centered at 450 nm could be explained by a ${}^1T_2 \leftarrow {}^1A_1$ transition of the $[\text{CrO}_4]^{2-}$ anion, red-shifted in the silver salt.^{3,4} Regarding its crystal structure, Ag_2CrO_4 crystallizes in orthorhombic space group $Pnma$ (no. 62), with lattice constants $a = 10.063(11)$ \AA , $b = 7.029(4)$ \AA , and $c = 5.540(2)$ \AA and four formula units per cell ($Z = 4$) under ambient conditions.⁵ The topology of this structure is typically described as consisting of isolated chromate $[\text{CrO}_4]$ groups whose oxygen atoms are coordinated to the silver atoms to generate a tridimensional network (Figure 1). Two different types of silver-centered oxygen polyhedra exist: elongated octahedra and distorted off-centered tetrahedra. This crystal structure is also adopted by Ag_2MnO_4 ,⁶ and as Chang and Jansen already pointed out, "in spite of similar lattice constants and identical space group this

compound is not isostructural to olivine Mg_2SiO_4 ⁷ or Al_2BeO_4 .⁸ The structures of some alkaline metal chromates such as potassium,⁹ rubidium,¹⁰ and cesium¹¹ also differ significantly from that of silver chromate even if described in the same space group. Compared to these compounds, the shorter metal–oxygen distances of silver chromate point to a greater degree of covalent bonding between cations and anions.¹²

Few experimental studies on Ag_2CrO_4 at high temperature (HT) or high pressure (HP) have been reported.^{13–16} A reversible first-order structural transformation was observed at 490 $^\circ\text{C}$ by differential thermal analysis, electrical conductivity measurements, and temperature-variable X-ray diffraction.^{13,14,16} The HT phase appears to be hexagonal with $Z = 16$ and lattice parameters $a = 9.92(4)$ \AA and $c = 19.76(8)$ \AA at 506 $^\circ\text{C}$.¹³ The phase diagram of silver chromate was studied by

Received: February 12, 2013

Revised: May 14, 2013

Published: May 14, 2013

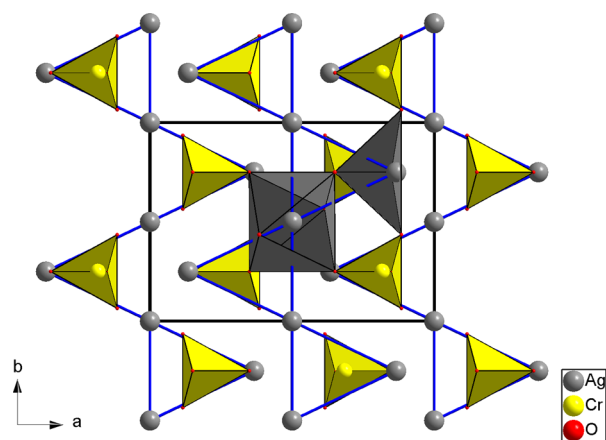


Figure 1. Projection along the c axis of the low-pressure $Pnma$ phase of silver chromate. Coordination polyhedra around the Ag and Cr atoms are depicted in gray and yellow, respectively.

Pistorius up to 4 GPa and 900 °C, and besides the aforementioned HT phase, no additional polymorphs were found.^{15,16} With regard to polymorphism under extreme conditions, a complementary description of the silver chromate structure based on the topology of its cation Ag_2Cr subarray could be relevant.¹⁷ This cationic framework adopts the Ni_2In structural type, formed by trigonal prisms of Ag atoms connected by common edges forming straight chains that run parallel to the bc plane (Figure 1). Adjacent chains of prisms are shifted $1/2c$ along this axis. The Cr atoms ($[CrO_4]$ groups) are located in the center of such prisms. Alkaline metal chromates of K, Rb, and Cs adopt a different structure (Co_2Si -type) that also consists of trigonal prisms of metal atoms but in a zigzag configuration. This alternative view of crystal structures of oxides, together with the well-established fact that cations in oxides tend to reproduce the structure of high-pressure phases of the corresponding (or chemically related) alloy, could provide a tool to predict new pressure-induced phases qualitatively.¹⁷ Thus, high-pressure studies on several oxides have shown that high-pressure transformations involve an increase in the number of neighboring atoms in their second coordination sphere,^{18–20} with their cation sublattice following the structural path expected for their corresponding alloys. Consequently, the behavior of M_2X compounds (where M = group IA or IB elements) under compression^{21–27} could give some hints of the potential transition mechanisms in Ag_2CrO_4 . Possible structural similarities with related chemical ternary oxides $A_2B^{VI}O_4$ should also be considered.

Taking this background into account, we aim in this work to give a detailed picture of the structure and physical properties of silver chromate up to 20 GPa. Angle-dispersive X-ray diffraction (ADXRD), Raman spectroscopy, and optical absorption measurements suggest that the initial orthorhombic phase undergoes an isostructural transition with a volume decrease of 1% at 4.5 GPa and a subsequent transition above 13 GPa. Preliminary first-principles calculations are unable to reproduce the isostructural phase transition.

2. EXPERIMENTAL DETAILS

Commercial silver chromate powder with 99.9% purity (Alfa Aesar, product no. 7784-01-2) was crushed in a mortar to obtain micrometer-sized samples. These samples were used to

carry out HP-ADXRD, HP-Raman, and HP-optical absorption measurements at room temperature.

2.1. ADXRD Experiments. Three independent HP-ADXRD experiments were conducted in diamond-anvil cells up to 20 GPa. Experiment 1 was carried out using an in-house Xcalibur diffractometer with Mo $K\alpha$ radiation ($\lambda = 0.7107$ Å). The same setup was previously used successfully to characterize the high-pressure phases of other compounds in the same pressure range.^{24–26} Experiments 2 and 3 were performed at the I15 beamline of Diamond and the MSPD beamline²⁸ of ALBA synchrotron light sources, respectively, with a 40×40 μm^2 -focused incident monochromatic beam of 0.4246 Å. The Ag_2CrO_4 metallic-luster powder samples were loaded into a 150- μm -diameter hole of a stainless-steel gasket preindented to a thickness of about 40 μm . A 16:3:1 methanol/ethanol/water mixture was used as a pressure-transmitting medium. Preliminary data reduction was done using the Fit2D software.²⁹ Pressure was measured by three different methods: (i) the ruby fluorescence scale;³⁰ (ii) the equation of state (EOS) of silver,³¹ which was added as an external pressure calibrant in experiments 1 and 2; and (iii) the EOS of copper³² in experiment 3. These methods give a maximum pressure uncertainty of 0.2 GPa at the highest pressure of this study (three ruby chips were evenly distributed in the pressure chamber). The observed intensities were integrated as a function of 2θ in order to give 1D diffraction profiles. The indexing and refinement of the powder diffraction patterns were performed using the FULLPROF³³ and POWDER-CELL³⁴ program packages.

2.2. Raman Experiments. Unpolarized HP-Raman scattering measurements at room temperature were performed on powder samples in backscattering geometry with a LabRAM HR UV microspectrometer coupled to a Peltier-cooled CCD camera. A 632.81 nm (1.96 eV) HeNe laser excitation line with a power of around 10 mW and a spectral resolution better than 2 cm^{-1} were used. During Raman experiments, samples were checked by monitoring the time dependence of the Raman signal at different accumulations and by visual inspection before and after each measurement in order to be sure that no heating effects occur during the measurements by the incoming laser excitation because the laser energy was above the band gap energy (1.75 eV (ref 35), 1.8 eV from our data). To analyze the Raman spectra, we have fit Raman peaks to a Voigt profile (Lorentzian profile convoluted by a Gaussian profile) where the spectrometer resolution is taken as a fixed Gaussian width (1.5 cm^{-1}). For HP studies, the samples were loaded into a membrane-type DAC. A 16:3:1 methanol/ethanol/water mixture was used as pressure-transmitting medium using the ruby fluorescence scale.³⁰

2.3. Optical Absorption Measurements. For optical absorption studies, we used 20- μm -thick polycrystal platelets. These platelets were obtained by compressing the Ag_2CrO_4 powder to 1 GPa using a large-volume press equipped with Bridgman anvils and using a hexagonal boron nitride disc as a pressure medium and to isolate the sample from the tungsten carbide anvils.³⁶ Measurements in the visible–near-infrared range were made with an optical setup that consisted of a tungsten lamp, fused silica lenses, reflecting optics objectives, and a visible–near-infrared spectrometer.³⁷ For HP-optical absorption studies, the samples were loaded in a membrane-type DAC with a similar configuration as in HP-ADXRD and HP-Raman experiments. The optical absorption spectra were

obtained from the transmittance spectra of the sample, which were recorded using the sample-in, sample-out method.^{38,39}

The three aforementioned techniques provide a comprehensive view of the structural, vibrational, and optical properties of silver chromate at ambient temperature and high pressures. In particular, the crystal structure, Raman-active phonons, and electronic band gap have been accurately determined.

2.4. First-Principles Calculations. Total-energy ab initio simulations have been performed within the density-functional theory (DFT) framework as implemented in the Vienna ab initio simulation package (VASP). (See refs 40 and 41 and references therein.) The program performs ab initio structural calculations with the plane wave pseudopotential method. The set of plane waves employed extended up to a kinetic energy cutoff of 520 eV. Such a large cutoff was required to achieve highly converged results within the projector-augmented-wave (PAW) scheme.^{41,42} The PAW method takes into account the full nodal character of the all-electron charge density distribution in the core region. The exchange-correlation energy was taken in the generalized gradient approximation (GGA) with the Perdew–Burke–Ernzerhof (PBE) prescription.⁴³ It is well known that the GGA approach typically underestimates the cohesion energy⁴⁴ (in turn, producing an overestimation of the equilibrium volume). We used dense special point grids appropriate to each structure considered to sample the Brillouin zone (BZ), thus ensuring a high convergence of 1 to 2 meV per formula unit in the total energy of each structure as well as an accurate calculation of the forces over the atoms. At each selected volume, the structures were fully relaxed to their equilibrium configurations through the calculation of the forces on atoms and the stress tensor.⁴⁴ It is useful to note that theoretical pressure, $P(V)$, can be obtained within the DFT formalism at the same time as the total energy, $E(V)$, but independently: P (like other derivatives of the energy) can be obtained from the calculated stress. In the relaxed theoretical equilibrium ($P = 0$ GPa) configuration, the forces were smaller than 0.006 eV/Å, and the deviation of the stress tensor from a diagonal hydrostatic form was less than 0.1 GPa.

Lattice-dynamic calculations of phonon modes were performed at the zone center (Γ point) of the BZ. We used a direct force-constant approach (or supercell method)⁴⁵ that it is conceptually simple. These calculations provide information about the symmetry of the modes and their polarization vectors and allow us to identify the irreducible representations and the character of the phonon modes at the Γ point.

3. CRYSTAL STRUCTURE UNDER COMPRESSION

Figures 2 and 3 show the ADXRD data for Ag_2CrO_4 at several selected pressures in experiment 3. The other data sets present similar features. Under ambient conditions, the X-ray diffraction pattern corresponds to the orthorhombic $Pnma$ structure previously reported, with similar lattice parameters: $a = 10.065(4)$ Å, $b = 7.013(3)$ Å, and $c = 5.538(2)$ Å. ADXRD patterns can be indexed in the initial low-pressure (LP) orthorhombic phase up to 3.5 GPa. Atomic coordinates do not change significantly in this pressure range. For instance, the ADXRD pattern at 2.7 GPa was refined by the Rietveld method (Figure 2) to obtain the final atomic positions collected in Table 1. The evolution of the unit-cell volume and lattice parameters of this phase is shown in Figure 4a,b, respectively. It can be seen that the contraction of the lattice parameters is rather anisotropic. For instance, according to our experiments,

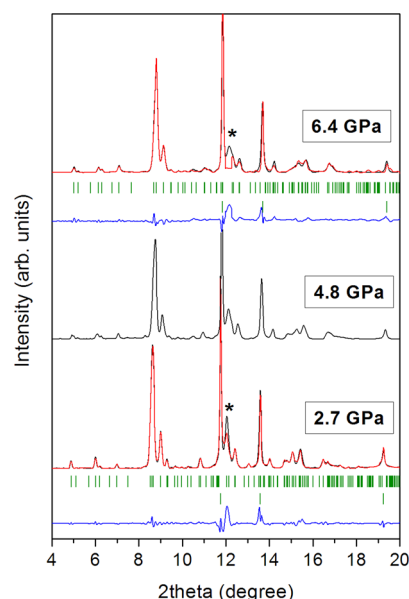


Figure 2. X-ray powder diffraction patterns of Ag_2CrO_4 at three selected pressures below 10 GPa. The calculated profiles and the residuals of the Rietveld refinements at 2.7 and 6.4 GPa are represented as red and blue lines, respectively. Vertical marks indicate the Bragg reflections of the orthorhombic $Pnma$ Ag_2CrO_4 structure and metallic copper, which was used as a second internal pressure calibrant. The asterisk marks the appearance of the most intense diffraction peak of the gasket.

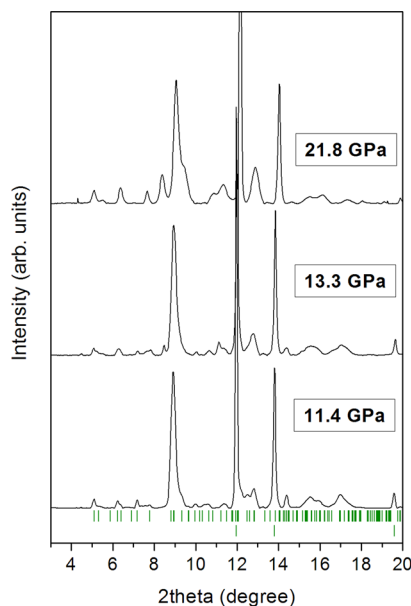


Figure 3. X-ray powder diffraction patterns of Ag_2CrO_4 at three selected pressures above 10 GPa. Vertical marks indicate the Bragg reflections of the orthorhombic $Pnma$ Ag_2CrO_4 structure and metallic copper at 11.4 GPa.

the relative contractions for a , b , and c between room pressure and 3.5 GPa are 1.51, 1.17, and 3.15%, respectively. A third-order Birch–Murnaghan EOS gives the following characteristic parameters: (i) a zero-pressure volume $V_0 = 391.3(3)$ Å³ and (ii) a bulk modulus $B_0 = 52(2)$ GPa and (iii) its first pressure derivative $B'_0 = 5.4(9)$. If B'_0 is fixed to 4, then $V_0 = 391.0(2)$ Å³ and $B_0 = 55.4(7)$ GPa. It is worth remembering that, even when considered to be an olivine-like structure in the ICSD

Table 1. Lattice Parameters and Rietveld-Refined Fractional Coordinates for the LP *Pnma* Phase at Ambient Pressure and 2.7 GPa and for the HP1 Phase at 6.4 GPa^a

	RP experiment	RP theory	2.7 GPa	6.4 GPa
<i>a</i> axis (Å)	10.065(4)	10.224	9.953(2)	9.682(3)
<i>b</i> axis (Å)	7.013(3)	7.025	6.9570(14)	6.862(2)
<i>c</i> axis (Å)	5.538(2)	5.653	5.4078(8)	5.3349(9)
unit-cell volume (Å ³)	390.9(4)	406.02	374.5(2)	354.4(3)
<i>x</i> _{Ag2}	0.1357(8)	0.1412	0.1364(9)	0.146(3)
<i>z</i> _{Ag2}	0.4916(14)	0.4827	0.5115(19)	0.522(3)
<i>x</i> _{Cr}	0.312(2)	0.3182	0.3130(19)	0.316(5)
<i>z</i> _{Cr}	1.003(3)	0.9633	0.983(5)	1.012(7)
<i>x</i> _{O1}	0.148(5)	0.1553	0.137(6)	0.149(19)
<i>z</i> _{O1}	0.919(8)	0.9051	0.974(13)	1.026(24)
<i>x</i> _{O2}	0.356(6)	0.3466	0.351(7)	0.389(11)
<i>z</i> _{O2}	0.265(9)	0.2558	0.270(12)	0.275(3)
<i>x</i> _{O3}	0.386(3)	0.3865	0.382(5)	0.441(7)
<i>y</i> _{O3}	0.442(4)	0.4429	0.454(5)	0.402(7)
<i>z</i> _{O3}	0.876(5)	0.8439	0.873(6)	0.940(9)

^aAg1 is located in 4a (0, 0, 0); Ag2, Cr, O1, and O2 are located in 4c (x, 0.25, z); and O3 is located in 8d (x, y, z).

database, the different chemical content of Ag₂CrO₄ generates a tilting movement of the [CrO₄] tetrahedra and the different *b/a* and *c/a* axis ratios cause two distinct coordination spheres for the silver atoms (coordination numbers of 6 and 4) instead of the quite regular [MgO₆] octahedra in olivine. This distribution of polyhedra and the fact that the Ag–O bonds are significantly more compressible than the Cr–O bonds make compression parallel to the *b* axis much more restricted than that parallel to *c*. The axial compressibility of related *Pnma* compounds differs considerably as a result of the different cation sizes and valences.^{8,46} Resultant bulk moduli also have a huge variability, from 242(5) GPa in Al₂BeO₄ chrysoberyl (*B'*₀ = 4, fixed)⁸ to the value obtained in this work for Ag₂CrO₄. Note also that the compressibility of K₂CrO₄, with a Co₂Si-type cation subarray, is significantly larger (*B*₀ = 26(2) GPa and *B'*₀ = 6.0(5)) than that of Ag₂CrO₄, with a Ni₂In-type cation network.⁴⁷

The LP phase starts to transform to a new HP phase (named HP1) at 3.5 GPa. The ADXRD patterns between this pressure and 5 GPa present five new low-intensity peaks below $2\theta = 8.4^\circ$ (synchrotron radiation) and some of the existing Bragg peaks slightly broaden. Diffractograms in this pressure range could not be unequivocally indexed, but the stability of the positions and intensities of most of the peaks suggests that only a small distortion of the lattice occurs. Between 5 and 12.5 GPa, the ADXRD patterns could be indexed in an orthorhombic cell whose reflection conditions are consistent with *Pnma* symmetry, similar to the ambient structure. The formation of this new phase entails a volume decrease of 0.95%, mainly caused by the 1.3% collapse of the *a* axis (Figure 4b). The LP structural model was used as a starting point for a Rietveld refinement. The HP1 phase (depicted in Figure 5) turned out to have the same structure as the LP phase. As shown in Table 1, the refinement suggests that the Ag₂Cr cation subarray seems not to change significantly, and only a strong distortion of the [CrO₄] tetrahedra is observed, with Cr–O distances at 6.4 GPa ranging from 1.565 to 1.84 Å (as compared to 1.58–1.74 Å at 2.7 GPa) and angles ranging from 70 to 132° (compare to 104–115° at 2.7 GPa). These O atomic displacements also entail the modification of the Ag-centered oxygen polyhedra.

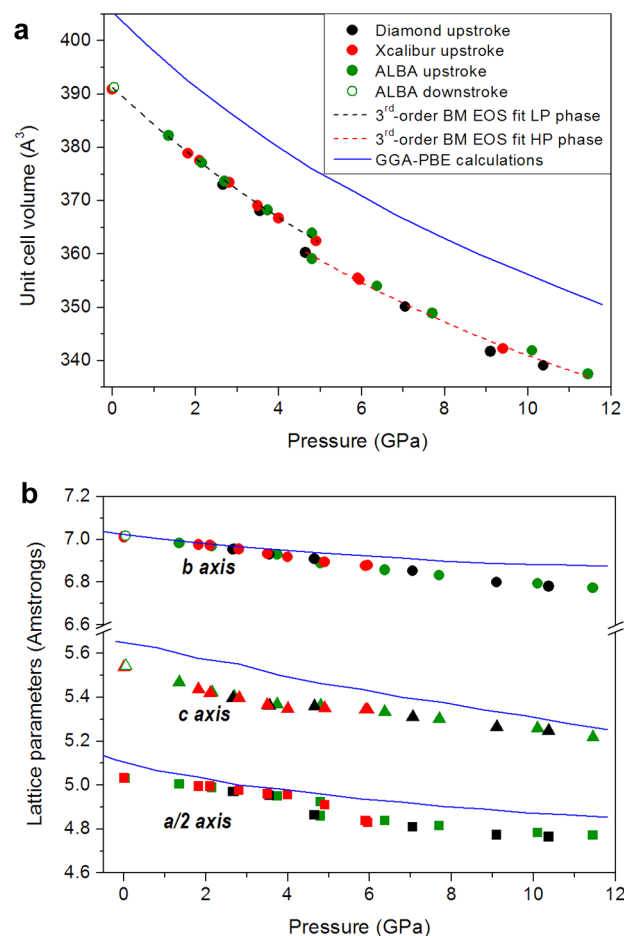


Figure 4. Evolution of the unit-cell volume (a) and the lattice parameters (b) of the low-pressure and the HP1 phases of Ag₂CrO₄ with pressure. Red, black, and green symbols correspond to XRD data according to Xcalibur, Diamond, and ALBA experiments, respectively. (b) *a/2*, *b*, and *c* axes are represented by squares, circles, and triangles, respectively. Dashed and solid lines correspond to fittings to our experimental data and results from theoretical calculations.

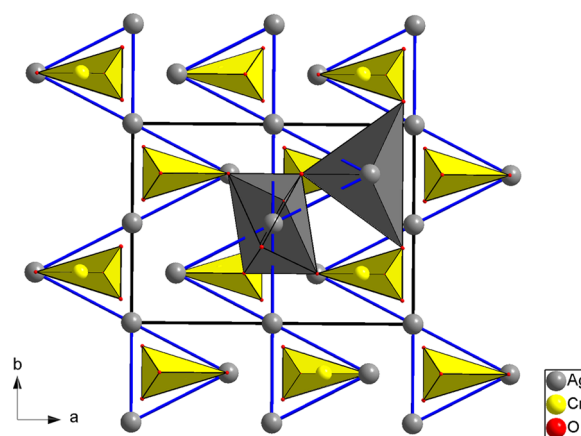


Figure 5. Projection along the *c* axis of the HP1 *Pnma* phase of silver chromate, to be compared to Figure 1. As can be seen, the cation Ag₂Cr subarray still adopts a Ni₂In-type structure, but the Ag and Cr coordination polyhedra are rather distorted.

The [AgO₆] octahedra are highly distorted, and their Ag–O distances decrease abruptly (from 2.39 to 2.27 Å on average), whereas the [AgO₄] tetrahedra become more regular and their

distances increase considerably (from 2.35 to 2.69 Å). The confirmation of such strong polyhedral distortions by single-crystal HP-ADXRD measurements is advisable. It is worth mentioning that the coexistence of the LP and HP1 phases would enable an explanation of two of the extra low-intensity peaks observed between 3.5 and 5 GPa as well as the apparent broadening of some reflections. The zero-pressure volume and the compressibility of the HP1 phase have been estimated by fixing the pressure derivative B'_0 to 4: $V_0 = 382(2) \text{ Å}^3$ and $B_0 = 69(3) \text{ GPa}$. This phase is a bit less compressible than the initial LP phase, with the continuous decrease in the lattice parameters being shown in Figure 4b.

Above 10 GPa, the diffraction peaks broaden significantly as a consequence of the loss of the quasi-hydrostatic conditions and the appearance of deviatoric stresses in the compressed sample⁴⁸ (Figure 3). These stresses could induce the second high-pressure phase (HP2) observed above 13 GPa. The limited quality of the X-ray patterns at these pressures hampers unequivocal indexation, but the small changes observed at the transition suggests either a sluggish transition resulting in the coexistence of the HP1 and HP2 phases over a large pressure range or a low-symmetry distortion of the HP1 orthorhombic phase. Both high-pressure phase transitions are reversible, and the LP phase is recovered after decompression with similar lattice constants: $a = 10.058(6) \text{ Å}$, $b = 7.018(4) \text{ Å}$, and $c = 5.542(3) \text{ Å}$ (Figure 4b).

4. LATTICE DYNAMICS UNDER COMPRESSION

Group theoretical considerations⁴⁹ indicate that the $Pnma$ structure of Ag_2CrO_4 has 36 Raman-active modes with mechanical representation $\Gamma = 11A_g + 7B_{1g} + 11B_{2g} + 7B_{3g}$, which can be also classified by factor group analysis as internal or external modes of the CrO_4 units so that there are 18 internal modes [$2\nu_1$, $4\nu_2$, $6\nu_3$, $6\nu_4$] and 18 external modes [6 rotational (R) and 12 translational (T)].¹² Therefore, the 36 Raman-active modes can be classified as $11A_g$ (ν_1 , ν_2 , $2\nu_3$, $2\nu_4$, R, 4T) + $7B_{1g}$ (ν_2 , ν_3 , ν_4 , 2R, 2T) + $11B_{2g}$ (ν_1 , ν_2 , $2\nu_3$, $2\nu_4$, R, 4T) + $7B_{3g}$ (ν_2 , ν_3 , ν_4 , 2R, 2T). Until now, only 12 Raman modes were measured for Ag_2CrO_4 at ambient conditions, likely because of the considerable overlapping of modes,¹² whereas 28 out of 42 Raman modes were measured for structurally related alkali chromates^{50,51} and 30 out of 36 Raman modes have been recently measured in monazite-type PbCrO_4 .⁵²

Figure 6 shows the Raman spectra of Ag_2CrO_4 at room temperature at selected pressures up to 18.8 GPa. The Raman spectrum of the LP phase is similar to that reported earlier.¹² The most intense Raman modes are the stretching modes of the CrO_4 group in the high-frequency region between 750 and 900 cm^{-1} .^{12,50,51} Of considerable weaker intensity are the bending modes of the CrO_4 group in the medium-frequency region between 300 and 400 cm^{-1} . Finally, translational and rotational lattice Raman modes in the low-frequency region below 150 cm^{-1} are the most difficult to identify. A change in the Raman spectrum can be clearly observed in both the medium- and high-frequency regions at 5 GPa (i.e., appearance/disappearance of Raman modes and/or discontinuous displacement of frequencies). This change is in good agreement with the phase transition suggested by ADXRD measurements at similar pressures. A more pronounced change in the Raman spectrum is observed above 14.8 GPa; this confirms the phase transition reported at around 14 GPa by ADXRD measurements. Raman measurements on the down-

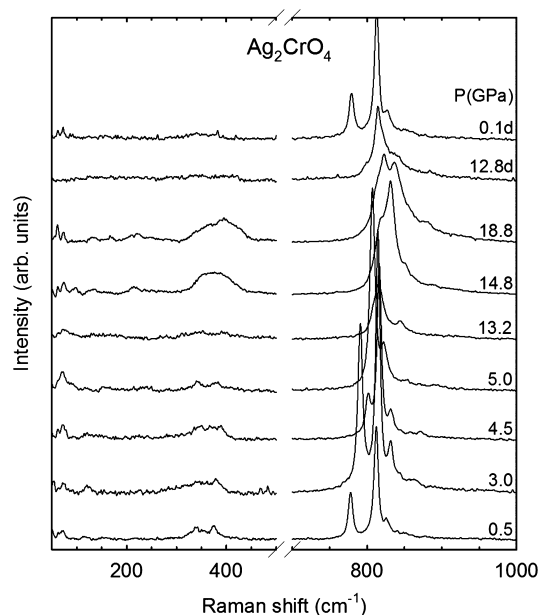


Figure 6. Raman scattering spectra of Ag_2CrO_4 at selected pressures up to 18.8 GPa on the upstroke and down to ambient pressure on the downstroke (d). Two reversible phase transitions at around 5 and 14 GPa have been observed.

stroke at 12.8 and 0.1 GPa confirm the reversibility of both phase transitions.

Figure 7 shows the pressure dependence of the measured Raman mode frequencies in Ag_2CrO_4 at room temperature up to 19 GPa. Experimental and calculated Raman modes for the LP phase are compared up to 5 GPa and show good agreement (Table 2). Table 3 summarizes the frequencies and pressure coefficients of the observed Raman modes for the HP1 and HP2 phases at 5 and 14 GPa, respectively. It can be observed

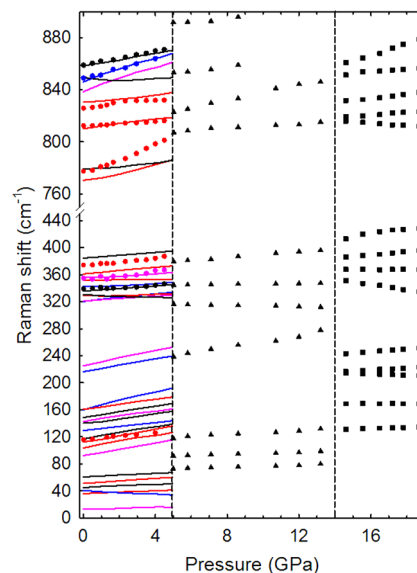


Figure 7. Pressure dependence of the Raman-active modes in Ag_2CrO_4 . Red, blue, black, and pink circles (experimental) and lines (theoretical) refer to A_g , B_{1g} , B_{2g} , and B_{3g} modes of the low-pressure phase, respectively. Raman-active modes of the HP1 and HP2 high-pressure phases above 5 and 14 GPa are noted with triangles and squares, respectively.

Table 2. Symmetries, Zero-Pressure Frequencies, and Pressure Coefficients of the Theoretical and Experimental Raman-Active Modes of the LP Phase of Ag_2CrO_4

	ω_0 (th.) (cm^{-1})	a (th.) ($\text{cm}^{-1}/\text{GPa}$)	ω_0 (exp.) (cm^{-1})	a (exp.) ($\text{cm}^{-1}/\text{GPa}$)		ω_0 (th.) (cm^{-1})	a (th.) ($\text{cm}^{-1}/\text{GPa}$)	ω_0 (exp.) (cm^{-1})	a (exp.) ($\text{cm}^{-1}/\text{GPa}$)
B_{3g}	13.1(1)	0.7(1)			B_{1g}	320.8(3)	2.7(1)		
A_g	36.3(1)	1.0(1)			B_{3g}	321.0(2)	1.8(1)		
B_{1g}	40.4(3)	−1.3(2)			A_g	328.3(6)	0.6(2)		
B_{2g}	45.6(3)	1.1(1)			B_{2g}	330.0(3)	−0.9(1)		
A_g	51.2(1)	1.8(1)			B_{2g}	335.6(1)	1.9(1)	338(2)	1.4(2)
B_{2g}	61.0(1)	1.3(1)			B_{1g}	342.0(6)	1.2(2)		
B_{3g}	92.2(2)	4.7(1)			A_g	351.9(1)	0.13(4)		
A_g	104.6(7)	4.5(1)			B_{3g}	354.9(5)	1.5(1)	353(2)	2.9(3)
A_g	112.0(3)	4.8(1)	116(1)	2.6(1)	A_g	361.1(2)	2.4(1)	373(1)	2.7(2)
B_{2g}	117.6(5)	4.4(2)			B_{2g}	384.4(1)	2.1(1)		
B_{1g}	129.5(1)	2.9(1)			A_g	769.4(6)	3.3(2)	776(1)	5.5(2)
B_{2g}	139.4(5)	3.7(2)			B_{2g}	778.5(5)	1.4(2)		
B_{3g}	143.5(6)	3.7(2)			A_g	810.4(3)	1.7(1)	812(1)	0.9(1)
B_{2g}	148.8(2)	4.2(1)			A_g	830.0(3)	1.5(1)	826(2)	1.5(1)
B_{1g}	161.0(6)	6.4(2)			B_{3g}	839.6(5)	4.4(2)		
A_g	161.8(2)	3.7(1)			A_g	847.1(5)	4.3(2)	849(3)	3.8(2)
B_{1g}	216.6(3)	4.7(1)			B_{2g}	849.2(8)	−0.1(1)		
B_{3g}	225.5(4)	5.5(1)			B_{2g}	858.3(2)	2.4(2)	859(3)	2.6(1)

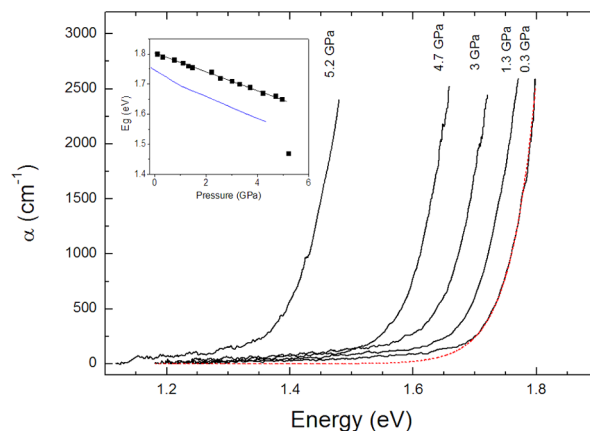
Table 3. Frequencies and Pressure Coefficients of the Experimental Raman-Active Modes of the HP1 and HP2 Phases of Ag_2CrO_4 at 5 and 14 GPa, Respectively, after Being Fit to Equation $\omega = \omega_0 + a^*P$

phase HP1 (5 GPa)			phase HP2 (14 GPa)		
mode	ω_0 (exp.) (cm^{-1})	a (exp.) ($\text{cm}^{-1}/\text{GPa}$)	mode	ω_0 (exp.) (cm^{-1})	a (exp.) ($\text{cm}^{-1}/\text{GPa}$)
1	73(2)	0.8(1)	1	131(1)	0.8(1)
2	92(2)	0.8(1)	2	170(1)	−0.03(1)
3	119(2)	1.5(1)	3	214(1)	−0.9(1)
4	239(3)	4.4(2)	4	216(1)	1.6(1)
5	316(2)	−0.5(1)	5	243(1)	2.1(1)
6	345(2)	0.3(1)	6	351(2)	−3.9(1)
7	379(2)	2.1(2)	7	368(2)	−0.08(1)
8	808(1)	0.9(1)	8	385(2)	2.5(1)
9	823(1)	2.9(1)	9	415(9)	3.6(5)
10	853(1)	1.6(2)	10	816(1)	−1.0(1)
			11	819(1)	1.1(1)
			12	831(2)	1.6(1)
			13	852(2)	1.1(2)
			14	859(3)	4.7(2)

that the frequencies of the stretching modes above 5 and 14 GPa are similar to those of the low-pressure phase, thus suggesting that there is no drastic change in coordination during the two phase transitions, at least for the Cr atom. However, the different pressure dependence of the Raman modes above 14 GPa does not support the coexistence of HP1 and HP2 phases in a region larger than 1 GPa. Furthermore, the larger number of Raman modes observed in the HP2 phase with respect to HP1 suggests that HP2 could be a low-symmetry distortion of the HP1 phase.

5. OPTICAL ABSORPTION UNDER COMPRESSION

Figure 8 shows the optical absorption spectra of Ag_2CrO_4 at room temperature and at selected pressures up to 5.2 GPa. Absorption spectra of the LP phase show a steep absorption characteristic of a direct band gap plus a low-energy absorption band that overlaps partially with the fundamental absorption.

**Figure 8.** Optical absorption spectrum of Ag_2CrO_4 at selected pressures up to 5.2 GPa. At 0.3 GPa, we also show in red the fundamental Urbach absorption to facilitate the identification of the low-energy absorption band described in the text (detectable for energy <1.7 eV). The inset shows the pressure dependence of the band gap energy compared to our theoretical DFT calculations (solid blue line) using a Hubbard term value of $U = 6$.

This absorption band has been previously observed in related oxides and seems to be caused by the presence of defects or impurities.⁵³ Its nature has been the subject of considerable debate and is beyond the scope of this work. Regarding the steep absorption edge, we found that it exhibits an exponential dependence on the photon energy following Urbach's law. Therefore, to determine the band gap energy, E_g , we have analyzed the measured absorption spectrum assuming $\alpha = A_0 \exp[-(E_g - \hbar\nu)/E_u]$. In this equation, E_u is Urbach's energy, which is related to the steepness of the absorption tail, and $A_0 = kE_u^{1/2}$ for a direct band gap, with k being a constant characteristic of the material. From the analysis of the spectrum collected at ambient pressure, we determined the band gap to be 1.8 eV in good agreement with previous studies.³⁵

In Figure 8, it can be seen that upon compression the absorption edge gradually red shifts up to 4.7 GPa. At 5.2 GPa, an abrupt shift is detected, which produces the color change

from brown-red to dark brown, indicating the occurrence of a band gap collapse. We associated this change with the first transition detected at similar pressure in diffraction and Raman experiments. At 5.2 GPa, the absorption coefficient values, the absorption edge shape, and its steepness suggest that HP1- Ag_2CrO_4 is also a direct band gap semiconductor. Unfortunately, at higher pressures we could not perform experiments because the sample deteriorates likely as a result of increasing intergrain strains, which prevented the collection of accurate optical data.

To analyze the pressure effects on the band gap of the LP phase qualitatively, we assumed that the LP and HP1 phases have a fundamental direct band gap. Using the same method employed to determine E_g under ambient conditions, we obtained the pressure dependence of E_g . The inset in Figure 8 shows the variation of E_g versus pressure up to 5.2 GPa. The LP phase shows a linear negative pressure coefficient of the band gap energy (-30 meV/GPa) up to the phase-transition pressure, which is in good agreement with ab initio band-structure calculations that give a pressure coefficient of -36 meV/GPa (inset in Figure 8). It is well known that DFT systematically underestimates the band gap. Different exchange-correlation functionals provide different values of the band gap, but the pressure evolution and the symmetry of the gap are usually well described.⁵⁴ We also conducted some tests using the DFT + U formalism, assuming a Hubbard term value of 6 for chromium. These calculations give a band gap similar to the experimental one at room pressure and a pressure coefficient similar to those obtained experimentally and using only DFT. From 4.7 to 5.2 GPa, E_g abruptly changes from 1.65 to 1.47 eV. Before discussing the pressure evolution of the band gap, we would like to mention that according to our calculations Ag_2CrO_4 is an indirect band gap material with the maximum of the valence band at the Γ point of the Brillouin zone and the minimum of the conduction band at the T point. Calculations established that the Γ – Γ direct band gap is 0.1 eV higher than the indirect band gap. This fact is in apparent contradiction with experiments. However, the energy difference between the direct and indirect gaps is small enough to make the indirect band gap undetectable by experiments in our samples because of the much higher absorption coefficient of the direct gap.

Upon the basis of our calculations, a knowledge of the electronic structure of Ag_2CrO_4 at atmospheric pressure, and the behavior of other chromates upon compression, a qualitative approach toward the understanding of the present results is suggested in the following text. According to the calculated electronic density of states (Figure 9), the main contribution to the bottom of the conduction band in Ag_2CrO_4 results from the antibonding interaction between the Cr 3d orbitals and the O 2p orbitals, and the upper portion of the valence band results primarily from the interaction between Ag 4d and O 2p orbitals. Under compression, Ag 4d states shift toward high energies faster than the Cr 3d states. This causes a reduction of the energy difference between the bottom of the conduction band and the top of the valence band, inducing the E_g reduction that we observed up to 4.7 GPa. According to calculations, both the direct and indirect gaps close with a similar pressure coefficient (-36 meV/GPa) in good agreement with experiments. Ouyang et al. calculations show a similar orbital dependence of the projection of the density of states at ambient pressure.³⁵ However, the collapse of E_g observed at 5.2 GPa could be caused by the structural change that we found at similar pressures. Although the structural changes do not affect

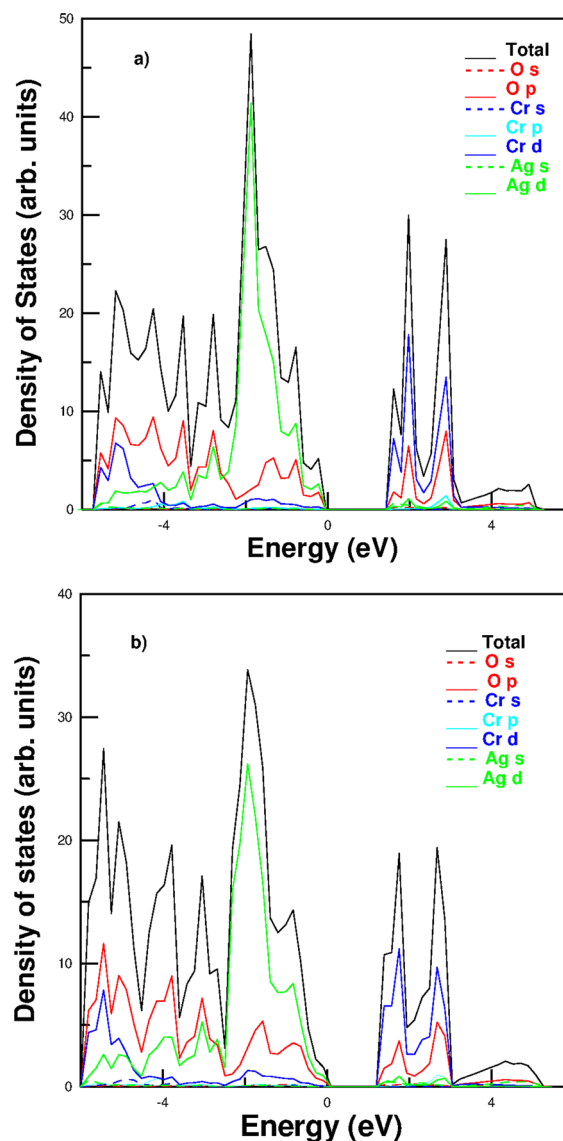


Figure 9. Orbital dependency of the density of states projection in Ag_2CrO_4 at two different pressures: (a) room pressure and (b) 4.25 GPa using PBE + U calculations ($U = 6$).

the global symmetry of the crystal, the crystal structure is highly distorted, affecting Cr–O and Ag–O bond angles and distances. These changes in the crystalline structure should be directly reflected in the electronic structure of Ag_2CrO_4 , producing the collapse of E_g that we observed.

6. STRUCTURAL FIRST-PRINCIPLES CALCULATIONS UNDER COMPRESSION

Total-energy (E) calculations as a function of volume were performed for six different high-pressure structural candidates of Ag_2CrO_4 . The choice of these potential phases is justified by (i) the expected analogy with the pressure-induced sequence in M_2X compounds (thenardite (Na_2SO_4 -type, $Fddd$)⁵⁵ and spinel (Na_2MoO_4 -type, $Fd-3m$)),⁵⁶ (ii) the expected analogy with pressure-induced transformations in olivine (wadsleyite ($Imma$), spinel),^{57,58} or (iii) possible structural similarities with chemically related compounds (spinel Ag_2MoO_4 ⁵⁹ or Ag_2WO_4 ,⁶⁰ high-temperature $Pn2n$ polymorph of Ag_2WO_4 ,⁶¹ $Pnma$ K_2CrO_4 -type⁹ or $Pbnn$ Na_2CrO_4 -type⁶²).

After performing a full optimization of the lattice parameters and atomic positions, we found that, as expected, the initial *Pnma* phase is the structure of Ag_2CrO_4 with the lowest enthalpy at ambient pressure. A fit with a Birch–Murnaghan third-order equation of state (EOS) gives the following characteristic parameters in good agreement with experimental results: $V_0 = 408.2 \text{ \AA}^3$, $B_0 = 50.2 \text{ GPa}$, and $B'_0 = 5.7$ (Figure 4). Equilibrium volume V_0 is overestimated by $\sim 4\%$, as usual with the GGA approximation. Our first-principles calculations using the GGA approximation do not predict any volume collapse in the initial *Pnma* structure at high pressures. The addition of on-site repulsion Hubbard term U to Ag and Cr atoms did not help to reproduce the structural behavior of the orthorhombic Ag_2CrO_4 phase. Therefore, experiments and calculations seem to indicate that a new structural and electronic description is required to model the properties of silver chromate. Low-symmetry subgroups of the initial Ag_2CrO_4 phase (space group nos. 31, 26, 19, 14, and 11) were also considered to be HP candidates, but after the relaxation of the lattice parameters and the atomic coordinates, all of them could be described within a *Pnma* space group.

Only the spinel-type structure has been found to be energetically competitive at high pressures for silver chromate (Figure 10 and Table 4). The spinel-type structure, with cubic

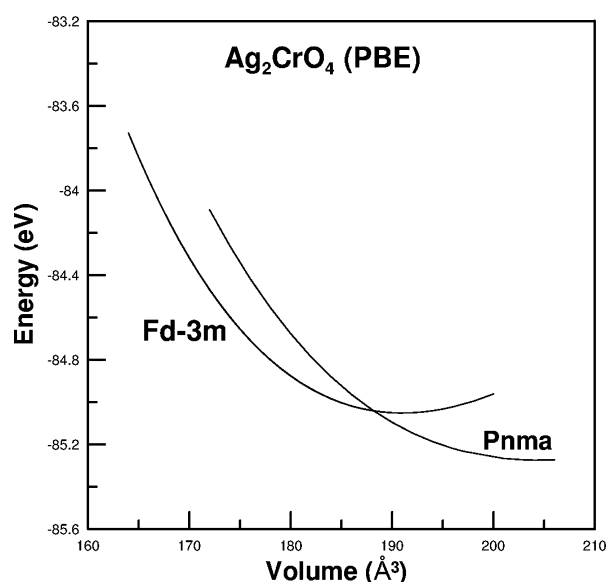


Figure 10. Energy as a function of volume curves for the initial *Pnma* phase and the spinel-type phase. Both curves cross each other at a volume corresponding to a pressure of 11 GPa. The energy and volume are written per formula unit.

Table 4. Lattice Parameters and Fractional Coordinates for the Spinel-Type Phase at 14.4 GPa, Predicted from First-Principles Calculations above 11 GPa^a

lattice parameter: $a = 8.759 \text{ \AA}$				
unit cell volume: $V = 672 \text{ \AA}^3$				
atom	Wyckoff position	x	y	z
Ag	16c	0	0	0
Cr	8b	0.375	0.375	0.375
O	32e	0.26508	0.26508	0.26508

^aS.G. *Fd-3m* (no. 227), origin choice 2.

symmetry, becomes more stable than the *Pnma* phase at a pressure of 11 GPa, after a first-order phase transition with a 2.7% decrease in volume. The spinel phase, however, has not been found experimentally in the pressure range covered in our experiments. This may be caused by the presence of kinetic-energy barriers or temperature effects that avoid the transformation.

7. CONCLUDING REMARKS

Three different characterization techniques (i.e., X-ray diffraction, optical absorption, and Raman spectroscopy) evidence the existence of two pressure-induced phase transitions in silver chromate at 4.5 and 13 GPa. The first HP phase could be indexed by an orthorhombic cell similar to that adopted at ambient pressure. Atomic coordinates of Ag and Cr atoms did not change significantly. Only a considerable distortion of $[\text{CrO}_4]$ seems to take place, but the structure can still be described within the initial *Pnma* space group. Consequently, the transition can be considered to be an isostructural transition. A volume collapse of 1% occurs at the transition, mainly as a result of the drastic contraction of the a axis (1.3%). We note that a similar rare transition was also recently observed in another chromate—cubic perovskite PbCrO_3 —that suffers a large volume collapse in an isostructural transition.⁶³

A second phase transition occurs at $\sim 13 \text{ GPa}$ to an unknown structure that Raman and X-ray diffraction data suggest could be a low-symmetry intimately related polymorph. First-principles calculations have been unable to reproduce both phase transitions likely because of unknown electronic considerations in Ag and Cr atoms and, in the case of the second transition, the existence of nonhydrostatic conditions in the experiment. Instead, they predict a high-pressure transformation to the spinel structure at 11 GPa, which experimentally was not observed in the studied pressure range likely as a result of the existence of kinetic effects. Further high-pressure experiments in chemically related compounds with analogous network architectures are a stepping stone for future work.

AUTHOR INFORMATION

Corresponding Author

*E-mail: dsantamaria@quim.ucm.es. Phone: +34 96 3543881.

Notes

The authors declare no competing financial interest.

ACKNOWLEDGMENTS

This study was supported by the Spanish government MEC under grants MAT2010-21270-C04-01/03/04 and CTQ2009-14596-C02-01, by the Comunidad de Madrid and European Social Fund (S2009/PPQ-1551 4161893), by the MALTA Consolider Ingenio 2010 project (CSD2007-00045), and by the Vicerrectorado de Investigación y Desarrollo of the Universidad Politécnica de Valencia (UPV2011-0914 PAID-05-11 and UPV2011-0966 PAID-06-11). A.M. and P.R.-H. acknowledge computing time provided by Red Española de Supercomputación (RES) and MALTA-Cluster. J.A.S. acknowledges Juan de la Cierva Fellowship Program for its financial support. Diamond and ALBA Synchrotron Light Sources are acknowledged for provisions of beam time. We also thank Drs. Peral, Popescu, and Fauth for technical support.

REFERENCES

- (1) *Colour Index*, 3rd ed.; Society of Dyers and Colourists: Bradford, England, 1971.
- (2) Ramon y Cajal, S., Ed.; *Histologie du Système Nerveux de l'Homme et des Vertébrés*; A. Maloine: Paris, 1909–1911.
- (3) Robbins, D. J.; Day, P. Why is Silver Chromate Red? Polarized Electronic Spectrum of Chromate in Silver Sulfate. *Mol. Phys.* **1977**, *34*, 893–898.
- (4) Clark, R. J. H.; Dines, T. J. Raman, Resonance Raman, and Infrared Spectroscopy Study of Silver(I) Chromate. *Inorg. Chem.* **1982**, *21*, 3585–3588.
- (5) Hackert, M. L.; Jacobson, R. A. The Crystal Structure of Silver Chromate. *J. Solid State Chem.* **1971**, *3*, 364–368.
- (6) Chang, F. M.; Jansen, M. Darstellung und Kristallstruktur von Ag_2MnO_4 . *Z. Anorg. Allg. Chem.* **1983**, *507*, 59–65.
- (7) Birle, J. D.; Gibbs, G. V.; Moore, P. B.; Smith, J. V. Crystal Structures of Natural Olivines. *Am. Mineral.* **1968**, *53*, 807–824.
- (8) Hazen, R. M. High-Pressure Crystal Chemistry of Chrysoberyl Al_2BeO_4 : Insights on the Origin of Olivine Elastic Anisotropy. *Phys. Chem. Miner.* **1987**, *14*, 13–20.
- (9) Zachariasen, W. H.; Ziegler, G. E. The Crystal Structure of Potassium Chromate K_2CrO_4 . *Z. Kristallogr.* **1931**, *80*, 164–173.
- (10) Smith, H. W.; Colby, M. Y. The Crystal Structure of Rubidium Chromate Rb_2CrO_4 . *Z. Kristallogr.* **1941**, *103*, 90–95.
- (11) Miller, J. J. The Crystal Structure of Cesium Chromate Cs_2CrO_4 . *Z. Kristallogr.* **1938**, *99*, 32–37.
- (12) Carter, R. L. Vibrational Spectra of Ag_2CrO_4 . *Spectrosc. Lett.* **1972**, *5*, 401–406.
- (13) Natarajan, M.; Secco, E. A. Phase Transformation Studies in Silver and Thallium Chromates. *Can. J. Chem.* **1974**, *52*, 712–717.
- (14) Cieslak-Golonka, M. Thermal Decomposition and Spectroscopic Properties of Silver Chromate. *J. Therm. Anal.* **1992**, *38*, 2501–2513.
- (15) Pistorius, C. W. F. T.; Boeyens, J. C. A. Crystallographic Aspects of the Polymorphism of Silver Chromate and Selenate at High Pressures and Temperatures. *Z. Kristallogr.* **1970**, *372*, 263–267.
- (16) Pistorius, C. W. F. T. Phase Diagrams of Silver Sulfate, Silver Selenate and Silver Chromate to 40 kbar. *J. Chem. Phys.* **1967**, *46*, 2167–2171.
- (17) Vegas, A.; Jansen, M. Structural Relationships between Cations and Alloys: An Equivalence between Oxidation and Pressure. *Acta Crystallogr., Sect. B* **2002**, *58*, 38–51.
- (18) Santamaria-Perez, D.; Gracia, L.; Garbarino, G.; Beltran, A.; Chulia-Jordan, R.; Gomis, O.; Errandonea, D.; Ferrer-Roca, C.; Martinez-Garcia, D.; Segura, A. High-Pressure Study of the Behavior of Mineral Barite by X-ray Diffraction. *Phys. Rev. B* **2011**, *84*, 054102.
- (19) Santamaria-Perez, D.; Chulia-Jordan, R. Compression of Mineral Barite, BaSO_4 : A Structural Study. *High Pressure Res.* **2012**, *32*, 81–88.
- (20) Santamaria-Perez, D.; Kumar, R. S.; Dos Santos-Garcia, A. J.; Errandonea, D.; Chulia-Jordan, R.; Saez-Puche, R.; Rodriguez-Hernandez, P.; Muñoz, A. High-Pressure Transition to the Postbarite Phase in BaCrO_4 Hashemite. *Phys. Rev. B* **2012**, *86*, 094116.
- (21) Grzechnik, A.; Vegas, A.; Syassen, K.; Loa, I.; Hanfland, M.; Jansen, M. Reversible Antifluorite to Anticotunnite Phase Transition in Li_2S at high Pressures. *J. Solid State Chem.* **2000**, *154*, 603–611.
- (22) Vegas, A.; Grzechnik, A.; Syassen, K.; Loa, I.; Hanfland, M.; Jansen, M. Reversible Phase Transitions in Na_2S under Pressure: A Comparison with the Cation Array in Na_2SO_4 . *Acta Crystallogr., Sect. B* **2001**, *57*, 151–156.
- (23) Vegas, A.; Grzechnik, A.; Hanfland, M.; Muhle, C.; Jansen, M. Antifluorite to Ni_2In -Type Phase Transition in K_2S at High Pressures. *Solid State Sci.* **2002**, *4*, 1077–1081.
- (24) Santamaria-Perez, D.; Vegas, A.; Muehle, C.; Jansen, M. High-Pressure Experimental Study on Rb_2S : Antifluorite to Ni_2In -Type Phase Transitions. *Acta Crystallogr., Sect. B* **2011**, *67*, 109–115.
- (25) Santamaria-Perez, D.; Vegas, A.; Muehle, C.; Jansen, M. Structural Behaviour of Alkaline Sulfides under Compression: High-Pressure Experimental Study on Cs_2S . *J. Chem. Phys.* **2011**, *135*, 054511.
- (26) Santamaria-Perez, D.; Marques, M.; Chulia-Jordan, R.; Menendez, J. M.; Gomis, O.; Ruiz-Fuertes, J.; Sans, J. A.; Errandonea, D.; Recio, J. M. Compression of Silver Sulfide: X-ray Diffraction Measurements and Total-Energy Calculations. *Inorg. Chem.* **2012**, *51*, S289–S298.
- (27) Santamaria-Perez, D.; Morales-Garcia, A.; Martinez-Garcia, D.; Garcia-Domene, B.; Muhle, C.; Jansen, M. Structural Phase Transitions on AgCuS Stromeierite under Compression. *Inorg. Chem.* **2013**, *52*, 355–361.
- (28) Knapp, M.; Peral, I.; Nikitina, M.; Quispe, M.; Ferrer, S. Technical Concept of the Materials Science Beamline at ALBA. *Z. Kristallogr. Proc.* **2011**, *1*, 137–142.
- (29) Hammersley, A. P.; Svensson, S. O.; Hanfland, M.; Fitch, A. N.; Hausermann, D. Two-Dimensional Detector Software: From Real Detector to Idealised Image or Two-Theta Scan. *High Pressure Res.* **1996**, *14*, 235–248.
- (30) Mao, H. K.; Xu, J.; Bell, P. M. Calibration of the Ruby Pressure Gauge to 800-kbar under Quasi-Hydrostatic Conditions. *J. Geophys. Res. (Solid Earth Planets)* **1986**, *91*, 4673–4676.
- (31) Akahama, Y.; Kawamura, H.; Singh, A. K. A Comparison of Volume Compressions of Silver and Gold up to 150 GPa. *J. Appl. Phys.* **2004**, *95*, 4767–4771.
- (32) Dewaele, A.; Loubeyre, P.; Mezouar, M. Equations of State of Six Metals above 94 GPa. *Phys. Rev. B* **2004**, *70*, 094112.
- (33) Rodriguez-Carvajal, J. Recent Advances in Magnetic Structure Determination by Neutron Powder Diffraction. *Physica B* **1993**, *192*, 55–69.
- (34) Nolze, G.; Kraus, W. PowderCell 2.0 for Windows. *Powder Diff.* **1998**, *13*, 256–259.
- (35) Ouyang, S. X.; Li, Z. S.; Ouyang, Z.; Yu, T.; Ye, J. H.; Zou, Z. G. Correlation of Crystal Structures, Electronic Structures, and Photocatalytic Properties in a Series of Ag-based Oxides: AgAlO_2 , AgCrO_2 , and Ag_2CrO_4 . *J. Phys. Chem. C* **2008**, *112*, 3134–3141.
- (36) Errandonea, D. The Melting Curve of Ten Metals up to 12 GPa and 1600 K. *J. Appl. Phys.* **2010**, *108*, 033517.
- (37) Lacomba-Perales, R.; Errandonea, D.; Segura, A.; Ruiz-Fuertes, J.; Rodriguez-Hernandez, P.; Radescu, S.; Lopez-Solano, J.; Mujica, A.; Muñoz, A. A Combined High-Pressure Experimental and Theoretical Study of the Electronic Band-Structure of Scheelite-Type AWO_4 ($A = \text{Ca}, \text{Sr}, \text{Ba}, \text{Pb}$) Compounds. *J. Appl. Phys.* **2011**, *110*, 043703.
- (38) Panchal, V.; Errandonea, D.; Segura, A.; Rodriguez-Hernandez, P.; Muñoz, A.; Lopez-Moreno, S.; Bettinelli, M. The Electronic Structure of Zircon-Type Orthovanadates: Effects of High-Pressure and Cation Substitution. *J. Appl. Phys.* **2011**, *110*, 043723.
- (39) Errandonea, D.; Martinez-Garcia, D.; Lacomba-Perales, R.; Ruiz-Fuertes, J.; Segura, A. Effects of High Pressure on the Optical Absorption Spectrum of Scintillating PbWO_4 Crystals. *Appl. Phys. Lett.* **2006**, *89*, 091913.
- (40) Kresse, G.; Furthmüller, J. Efficient Iterative Schemes for Ab Initio Total-Energy Calculations Using a Plane-Wave Basis Set. *Phys. Rev. B* **1996**, *54*, 11169–11186.
- (41) Kresse, G.; Joubert, D. From Ultrasoft Pseudopotentials to the Projector Augmented-Wave Method. *Phys. Rev. B* **1999**, *59*, 1758–1775.
- (42) Blochl, P. E. Projector Augmented-Wave Method. *Phys. Rev. B* **1994**, *50*, 17953–17979.
- (43) Perdew, J. P.; Burke, K.; Ernzerhof, M. Generalized Gradient Approximation Made Simple. *Phys. Rev. Lett.* **1996**, *77*, 3865–3868.
- (44) Mujica, A.; Rubio, A.; Muñoz, A. High-Pressure Phases of Group-IV, III-V, and II-VI Compounds. *Rev. Mod. Phys.* **2003**, *75*, 863–912.
- (45) Parlinski, K.; Li, Z. Q.; Kawazoe, Y. First-Principle Determination of the Soft Mode in Cubic ZrO_2 . *Phys. Rev. Lett.* **1997**, *78*, 4063–4066.
- (46) Zhang, L. Single Crystal Hydrostatic Compression of $(\text{Mg}, \text{Mn}, \text{Fe}, \text{Co})_2\text{SiO}_4$ Olivines. *Phys. Chem. Miner.* **1998**, *25*, 308–312.

- (47) Edwards, C. M.; Haines, J.; Butler, I. S.; Leger, J.-M. High-pressure X-ray Diffraction Study of Potassium Chromate: Pressure-induced Orientational Disorder and its Implications for Amorphization in A_2BX_4 Compounds. *J. Phys. Chem. Solids* **1999**, *60*, 529–538.
- (48) Klotz, S.; Chervin, J. C.; Munsch, P.; Le Marchand, G. Hydrostatic Limits of 11 Pressure Transmitting Media. *J. Phys. D: Appl. Phys.* **2009**, *42*, 075413.
- (49) Kroumova, E.; Arroyo, M. I.; Perez-Mato, J. M.; Kirov, A.; Capillas, C.; Ivantchev, S.; Wondratschek, H. Bilbao Crystallographic Server: Useful Databases and Tools for Phase Transition Studies. *Phase Transitions* **2003**, *76*, 155–170.
- (50) Carter, R. L.; Bricker, C. E. Laser-Raman Spectra of Crystalline K_2CrO_4 , Rb_2CrO_4 and Cs_2CrO_4 . *Spectr. Acta* **1971**, *27A*, 569–580.
- (51) Serghiou, G.; Guillaume, C. Stability of K_2CrO_4 to 50 GPa Using Raman Spectroscopy Measurements. *J. Solid State Chem.* **2004**, *177*, 4672–4679.
- (52) Bandiello, E.; Errandonea, D.; Martinez-Garcia, D.; Santamaria-Perez, D.; Manjon, F. J. Effects of High-Pressure on the Structural, Vibrational, and Electronic Properties of Monazite-Type $PbCrO_4$. *Phys. Rev. B* **2012**, *85*, 024108.
- (53) Lacomba-Perales, R.; Ruiz-Fuertes, J.; Errandonea, D.; Martinez-Garcia, D.; Segura, A. Optical Absorption of Divalent Metal Tungstates: Correlation between the Band-Gap Energy and the Cation Ionic Radius. *Eur. Phys. Lett.* **2008**, *83*, 37002.
- (54) Fahy, S.; Chang, K. J.; Louie, S. G.; Cohen, M. L. Pressure Coefficient of Band-Gaps in Diamond. *Phys. Rev. B* **1987**, *35*, 5856–5859.
- (55) Nord, A. G. Refinement of the Crystal Structure of Thenardite, $Na_2SO_4(V)$. *Acta Chem. Scand.* **1973**, *27*, 814–822.
- (56) Becka, L. N.; Poljak, R. J. *An. Asoc. Quim. Argent.* **1958**, *46*, 204.
- (57) Haiber, M.; Ballone, P.; Parrinello, M. Structure and Dynamics of Protonated Mg_2SiO_4 : An Ab Initio Molecular Dynamics Study. *Am. Mineral.* **1997**, *82*, 913–922.
- (58) Horiuchi, H.; Sawamoto, H. β - Mg_2SiO_4 : Single-Crystal X-ray Diffraction Study. *Am. Mineral.* **1981**, *66*, 568–575.
- (59) Wyckoff, R. W. G. The Crystal Structure of Silver Molybdate. *J. Am. Chem. Soc.* **1922**, *44*, 1994–1998.
- (60) Van den Berg, A. J.; Juffermans, C. A. H. The Polymorphism of Silver Tungstate Ag_2WO_4 . *J. Appl. Crystallogr.* **1982**, *15*, 114–116.
- (61) Skarstad, P. M.; Geller, S. (W4O16)⁸⁻ Polianion in the High Temperature Modification of Silver Tungstate. *Mater. Res. Bull.* **1975**, *10*, 791–799.
- (62) Miller, J. J. The Crystal Structure of Anhydrous Sodium Chromate, Na_2CrO_4 . *Z. Kristallogr.* **1936**, *94*, 131–136.
- (63) Xiao, W.; Tan, D.; Xiong, X.; Liu, J.; Xu, J. Large Volume Collapse in the Phase Transition in Cubic $PbCrO_3$. *Proc. Natl. Acad. Sci. U.S.A.* **2010**, *107*, 14026–14029.